Mechanics of stretchable electronics on balloon catheter under extreme deformation

CrossMark

Yewang Su [a,b], Zhuangjian Liu [c], Shuodao Wang [d], Roozbeh Ghaffari [e], Dae-Hyeong Kim [f], Keh-Chih Hwang [a,g], John A. Rogers [d], Yonggang Huang [b,*]

[a] Center for Mechanics and Materials, Tsinghua University, Beijing 100084, China
[b] Department of Civil Engineering and Mechanical Engineering, Northwestern University, Evanston, IL 60208, USA
[c] Institute of High Performance Computing, A*Star 138632, Singapore
[d] Department of Materials Science and Engineering, University of Illinois, Urbana, IL 61801, USA
[e] MC10 Inc., Cambridge, MA 02140, USA
[f] Center for Nanoparticle Research of Institute for Basic Science, School of Chemical and Biological Engineering, Seoul National University, Seoul 151-742, Republic of Korea
[g] AML, Department of Engineering Mechanics, Tsinghua University, Beijing 100084, China

A B S T R A C T

Stretchable electronics has been applied to balloon catheters for high-efficacy ablation, with tactile sensing integrated on the surface, to establish full and conformal contact with the endocardial surface for elimination of the heart sink caused by blood flow around their surfaces. The balloon of the catheter folds into uniform 'clover' patterns driven by the pressure mismatch inside (~vacuum) and outside of the balloon (pressure ~1 atm). The balloon catheter, on which microelectrodes and interconnects are printed, undergoes extreme mechanical deformation during its inflation and deflation. An analytic solution is obtained for balloon catheter inflation and deflation, which gives analytically the distribution of curvatures and the maximum strain in the microelectrodes and interconnects. The analytic solution is validated by the finite element analysis. It also accounts for the effect of inflated radius, and is very useful to the optimal design of balloon catheter.

Crown Copyright © 2014 Published by Elsevier Ltd. All rights reserved.

1. Introduction

The major push in the electronics industry has always been toward smaller and faster devices. These hard, rigid and flat devices are confined to the planar surface of silicon wafers. Stretchable and flexible electronics have emerged to offer the performance of conventional wafer-based devices, but mechanical properties of a rubber band (e.g., Kim et al., 2010b; Rogers and Huang, 2009). This type of technology offers many new application opportunities, particularly for mounting on soft, elastic and curved objects, such as tissues of the human body (Kim et al., 2012b; Kim et al., 2010b). Examples range from cameras that use biologically inspired designs to achieve superior performance (Jin et al., 2004; Jung et al., 2011; Ko et al., 2008) and flexible sensors (Lumelsky et al., 2001; Mannsfeld et al., 2010; Someya et al., 2005; Someya and Sekitani, 2009; Takei et al., 2010), to surgical and diagnostic implements that naturally integrate with the human body to provide advanced therapeutic capabilities, such as conformal bio-integrated electronics for monitoring brain activities (Berger et al., 2001; Kim et al., 2010a); light-emitting sutures for accelerated wound healing and transducers of blood oxygenation and perfusion, waterproof micro-LEDs and proximity-sensor on surgical gloves to monitor distance from a proximal object, and illuminated plasmonic crystals and thin, refractive-index monitors on flexible tubing for intravenous delivery systems to monitor dosage of nutrition and medicines (Viventi et al., 2010a); conformal bio-interfaced silicon electronics for mapping cardiac electrophysiology (Baek et al., 2008; Kim et al., 2012a; Kim et al., 2011; Viventi et al., 2010b) and brain activities *in vivo* (Viventi et al., 2011); multifunctional balloon catheters for cardiac ablation therapy (Kim et al., 2012a; Kim et al., 2011); and epidermal electronics for the measurement of electrical activities produced by the heart (EKG), brain (EEG) and skeletal muscles (EMG) (Kim et al., 2011).

Kim et al. (2012a) demonstrated integrated stretchable electronics and tactile sensors on cardiac balloon catheters that were used to detect circumferential contact between the balloon surface and endocardial tissue during ablation treatment. These arrays of tactile sensors can help reduce dependence on intraprocedural X-ray and radioactive contrast agents, which are typically employed by physicians to help assess mechanical contact between balloon catheters and endocardial tissue. Tactile sensors on balloons provide a safe quantitative alternative to X-ray imaging during cardiac ablation procedures. In addition to assessing

mechanical contact, there are several other sensing modalities, including electrocardiograms, temperature, and pH mapping, which can be measured with stretchable electronics on balloons.

Mapping physiological parameters at specific anatomical targets, like the heart as well as other internal organs, requires that the flexible sensors, actuators and substrates of balloon catheters all fold down to their minimal geometric profile in order to allow safe insertion and routing through small arteries and veins. The balloons must therefore repeatedly transition from their original inflated state (shown in Fig. 1a), to fully deflated state (Fig. 1b). In their deflated state, the balloon substrate forms three 'clover-shaped lobes' (Figs. 1c and 1d), driven by a pressure mismatch between inside (∼vacuum) and outside of the balloon (pressure ∼1 atm). Three lobes occur most frequently, though four lobes have also been observed before. The lobes are far apart and have essentially no interactions. Through controlled inflation the balloon catheter then can be configured to match requirements on size and shape for its interaction with the tissue, where contact occurs in a soft, conformal manner, capable of accommodating complex, curvilinear and time dynamic surfaces in a completely non-destructive manner.

The balloon catheter undergoes extreme mechanical deformation during the inflation and deflation. It is important to ensure that the maximum strains in the microelectrodes and interconnects integrated on the balloon catheter are well below their fracture limit. An analytic mechanics model for the inflation and deflation of balloon catheter is established in Section 2. It is validated by the finite element analysis (FEA) that accounts for details of the microelectrodes, interconnects and balloon catheter. Application of the analytic model to the design of stretchable electronics for high-efficacy ablation is discussed in Section 3. The effect of initial radius of the inflated balloon catheter is also discussed in Section 3, together with the numerical results obtained from FEA.

2. Analytic model

As shown in Fig. 1a, the microelectrodes and interconnects are printed on a Dymax adhesive, which is attached to the balloon catheter around its equator. The polyurethane balloon catheter is 60 μm thick. Fig. 1e shows a representative cross section of interconnects on the balloon catheter, with a 20-μm-thick Dymax layer as the adhesive and a 60-μm-thick Dymax layer as the encapsulation, on top of the PI/Au/PI microelectrode. The microelectrodes are printed in pairs (Fig. 1a), and have the cross section similar to Fig. 1e but without the 60-μm-thick Dymax encapsulation and 1.2-μm-thick PI layer to expose Au. Within the pair of microelectrodes the Au layer is removed, which leaves only the 20-μm-thick Dymax adhesive and 4.2-μm-thick PI layer. Beyond the pair of microelectrodes there is only 80-μm-thick Dymax layer (60-μm encapsulation +20-μm adhesive).

As to be discussed in Section 3, these cross sections, together with 60-μm-thick balloon catheter, have similar bending stiffness. Therefore they can be approximated by a uniform beam with the effective thickness h and effective bending stiffness EI (per unit width) to be given in Section 3. As shown in Fig. 2a, each lobe is modeled as a beam, subject to external pressure p and bent to the shape of a "tennis racket", similar to the experiments (Fig. 1c). This deformation mechanism is similar to the collapse (Elliott et al., 2004; Pugno, 2010) and self-folding (Buehler, 2006; Buehler et al., 2004; Falvo et al., 1997; Zhou et al., 2007) of carbon nanotubes, though the latter is driven by Van der Waals force. The initial radius of the fully inflated balloon catheter (∼10 mm) is much larger than the bend radius (∼0.2 mm) of "tennis racket" such that the initial curvature of beam is neglected and is considered initially flat. These approximations of uniform, initially flat beam are validated by FEA in Section 3.
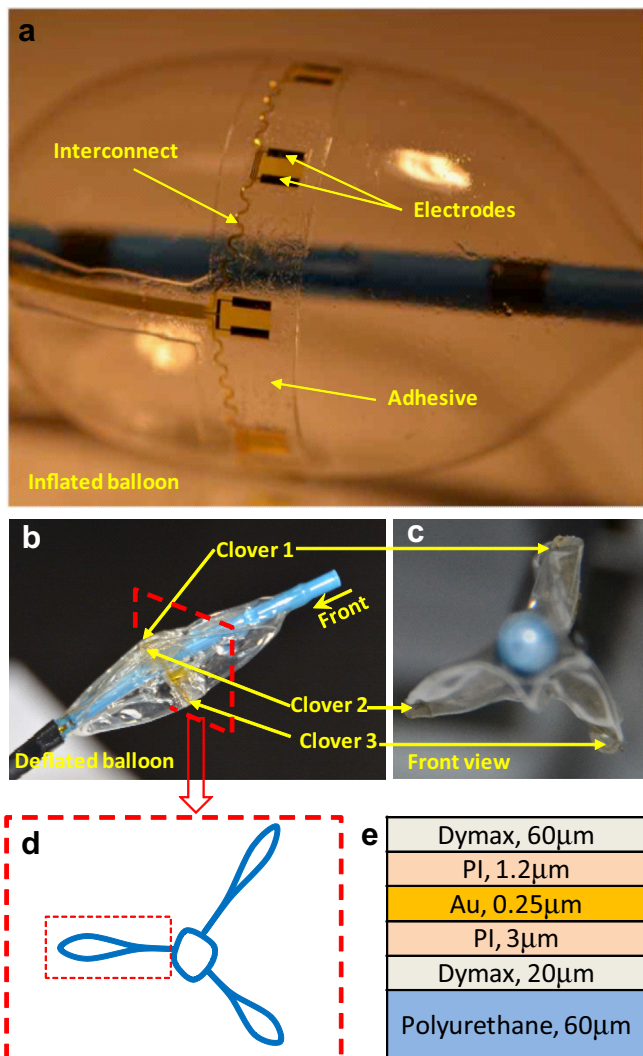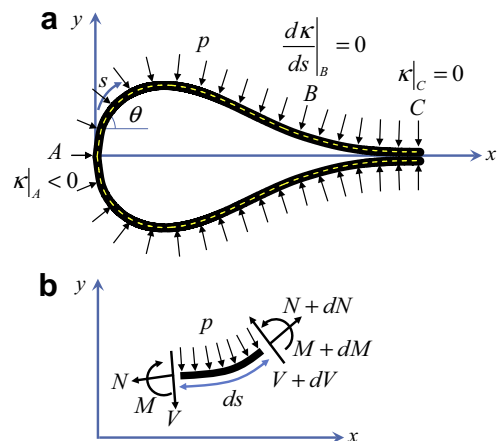

Fig. 1. (a) Inflated balloon catheter; (b) deflated balloon catheter; (c) a view of the deflated balloon catheter along its axial direction; (d) a schematic illustration of uniform 'clover' patterns for the deflated balloon catheter; (e) a representative cross section of interconnects on the balloon catheter.

Fig. 2. (a) A schematic diagram of a beam bent to the shape of a "tennis racket" under the external pressure p; (b) illustration of axial and shear forces, bending moment and external pressure.

Let N, V and M (Fig. 2b) denote the axial force, shear force and bending moment in the beam (per unit width), respectively. Equilibrium of bending moment and forces gives

$$\frac{dM}{ds} + V = 0,$$
$$\frac{dV}{ds} + N\frac{d\theta}{ds} - p = 0, \qquad (1a, b, c)$$
$$\frac{dN}{ds} - V\frac{d\theta}{ds} = 0,$$

where s is the arc length and θ is the angle of rotation (Fig. 2a), which is related to curvature κ by $\kappa = d\theta/ds$. The relation between bending moment and curvature $M = EI\kappa$, together with Eq. (1a), gives the shear force $V = -EId\kappa/ds$. Its substitution into Eq. (1c) and then integration gives

$$N = N_0 - \frac{1}{2}EI\kappa^2, \qquad (2)$$

where the constant of integration N_0 represents the axial force where the curvature is zero, and is to be determined. Eq. (1b) then becomes

$$\frac{d^2\kappa}{ds^2} + \frac{1}{2}\kappa^3 - \frac{N_0}{EI}\kappa + \frac{p}{EI} = 0, \qquad (3)$$

which can be integrated to give

$$\left(\frac{d\kappa}{ds}\right)^2 + \frac{1}{4}\kappa^4 - \frac{N_0}{EI}\kappa^2 + \frac{2p}{EI}\kappa = D, \qquad (4)$$

where the constant of integration D is to be determined.

It should be pointed out the exact shape of the deflection curve of a flexible member is called the Elastica (Fertis, 1999; Timoshenko and Gere, 1961). The most well-known Elastica is for a flexible uniform cantilever beam subject to a concentrated load at the free end. A few other Elastica solutions also exist (Fertis, 1999), but all are limited to statistically determinate beams. No Elastica solution exist for statistically indeterminate structures, as in the present study for a beam subject to the external pressure p that remains normal to the deformed beam.

For the "tennis racket" shape in Fig. 2a, only the upper half ($y > 0$) is studied due to symmetry. At the symmetry point A, the symmetry conditions are (Fig. 2a)

$$y(s = 0) = 0,$$
$$\theta(s = 0) = \frac{\pi}{2}, \qquad (5a, b, c)$$
$$V(s = 0) = 0,$$

where the coordinate y is shown in Fig. 2a, and $V(s = 0) = 0$ is equivalent to $d\kappa/ds(s = 0) = 0$. At the end of bent beam C (Fig. 2a), the coordinate y is $h/2$ due to contact with the bottom half of the beam, and the angle of rotation is zero,

$$y(s = L) = \frac{h}{2},$$
$$\theta(s = L) = 0, \qquad (6a, b)$$

where the length of bent beam, L, is to be determined by the condition of vanishing bending moment

$$M(s = L) = 0, \qquad (7)$$

or equivalently, $\kappa(s = L) = 0$. Eq. (7) results from the continuity of bending moment across C since the flat beam (to the right of C, Fig. 2a) gives a vanishing curvature.

As shown in the Appendix A, equilibrium Eqs. (1b,c) and boundary conditions (5a) and (6a) give

$$N_0 = -\frac{ph}{2}. \qquad (8)$$

This is equivalent to the equilibrium of force along the x direction since N_0 is the axial force at C at which the curvature is zero.

For the "tennis racket" shape in Fig. 2a, the curvature at the symmetry point A is negative, and is denoted by $\kappa_{\min}$ (<0), which is also the minimal curvature in the entire beam. The curvature initially increases with the arc length s from A, becomes positive and reaches a maximum $\kappa_{\max}$ at a point B between A and C, and eventually decreases to approaches zero at the end C [as given in Eq. (7)]. Substitution of $d\kappa/ds = 0$ at A from Eq. (5c) into Eq. (4) gives the constant of integration

$$D = \frac{1}{4}\kappa_{\min}^4 + \frac{ph}{2EI}\kappa_{\min}^2 + \frac{2p}{EI}\kappa_{\min}. \qquad (9)$$

Similarly, $d\kappa/ds = 0$ at B gives the first equation to determine $\kappa_{\min}$ and $\kappa_{\max}$ as

$$\kappa_{\max}^4 - \kappa_{\min}^4 + \frac{2ph}{EI}\left(\kappa_{\max}^2 - \kappa_{\min}^2\right) + \frac{8p}{EI}(\kappa_{\max} - \kappa_{\min}) = 0. \qquad (10)$$

Eq. (4) can then be written as

$$\frac{d\kappa}{ds} = \pm\frac{1}{2}\sqrt{\kappa_{\min}^4 - \kappa^4 + \frac{2ph}{EI}\left(\kappa_{\min}^2 - \kappa^2\right) + \frac{8p}{EI}(\kappa_{\min} - \kappa)}. \qquad (11)$$

where "+" is for the arc between A and B, and "−" is between B and C. Eqs. (5b) and (6b) give $\int_A^C d\theta = \int_A^C \kappa\, ds = -\frac{\pi}{2}$, which, together with Eq. (11), gives the second equation to determine $\kappa_{\min}$ and $\kappa_{\max}$ as

$$\int_{\kappa_{\min}}^{\kappa_{\max}} \frac{\kappa}{\sqrt{\kappa_{\min}^4 - \kappa^4 + \frac{2ph}{EI}\left(\kappa_{\min}^2 - \kappa^2\right) + \frac{8p}{EI}(\kappa_{\min} - \kappa)}}d\kappa$$
$$+ \int_0^{\kappa_{\max}} \frac{\kappa}{\sqrt{\kappa_{\min}^4 - \kappa^4 + \frac{2ph}{EI}\left(\kappa_{\min}^2 - \kappa^2\right) + \frac{8p}{EI}(\kappa_{\min} - \kappa)}}d\kappa = -\frac{\pi}{4}. \qquad (12)$$

Eqs. (10) and (12) constitute two equations for $\kappa_{\min}$ and $\kappa_{\max}$. Dimensional analysis gives the scaling law, i.e., the structure of their solution, as

$$\kappa_{\min} = \left(\frac{8p}{EI}\right)^{1/3}\bar{\kappa}_{\min}(\bar{h}), \quad \kappa_{\max} = \left(\frac{8p}{EI}\right)^{1/3}\bar{\kappa}_{\max}(\bar{h}), \qquad (13)$$

where

$$\bar{h} = \left(\frac{8p}{EI}\right)^{1/3}h \qquad (14)$$

is the normalized beam thickness, and $\bar{\kappa}_{\min}$ and $\bar{\kappa}_{\max}$ are non-dimensional functions of $\bar{h}$ determined from

$$\bar{\kappa}_{\max}^4 - \bar{\kappa}_{\min}^4 + \frac{\bar{h}}{4}\left(\bar{\kappa}_{\max}^2 - \bar{\kappa}_{\min}^2\right) + \bar{\kappa}_{\max} - \bar{\kappa}_{\min} = 0, \qquad (15)$$

and

$$\int_{\bar{\kappa}_{\min}}^{\bar{\kappa}_{\max}} \bar{\kappa}f\left(\bar{\kappa}; \bar{\kappa}_{\min}, \bar{h}\right)d\bar{\kappa} + \int_0^{\bar{\kappa}_{\max}} \bar{\kappa}f\left(\bar{\kappa}; \bar{\kappa}_{\min}, \bar{h}\right)d\bar{\kappa} = -\frac{\pi}{4}, \qquad (16)$$

where

$$f\left(\bar{\kappa}; \bar{\kappa}_{\min}, \bar{h}\right) = \left[\bar{\kappa}_{\min}^4 - \bar{\kappa}^4 + \frac{\bar{h}}{4}\left(\bar{\kappa}_{\min}^2 - \bar{\kappa}^2\right) + \bar{\kappa}_{\min} - \bar{\kappa}\right]^{-1/2}. \qquad (17)$$

Numerical results of Eqs. (15) and (16) are shown in Fig. 3. For a rectangular cross section subject to 1 atm, $\bar{h}$ is independent of beam thickness and is given by $\bar{h} = (96\text{ atm}/E)^{1/3}$, which ranges from 0.042 for silicon ($E = 130$ GPa) to 1.7 for PDMS ($E = 2$ MPa). For small $\bar{h}$, the above two equations can be solved by the method of perturbation as (see Appendix A for details)

$$\bar{\kappa}_{\min} = -1.053 + 0.08143\bar{h}, \quad \bar{\kappa}_{\max} = 0.1745 - 0.02853\bar{h}. \qquad (18)$$

As shown in Fig. 3, the perturbation solution agrees very well with the numerical solution for the full range of $\bar{h}$.
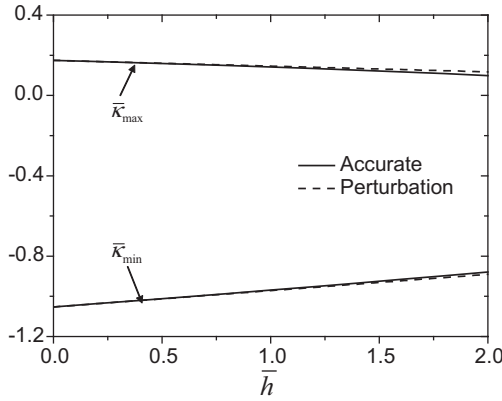
Fig. 3. The normalized maximum and minimum curvatures versus the normalized beam thickness when bent to the shape of a "tennis racket" under the external pressure p. Both the accurate and perturbation solutions are shown.

The arc length s can be obtained analytically as a function of κ, $s = s(\kappa)$, by integrating Eq. (11),

$$s(\bar{\kappa}) = \begin{cases} \left(\frac{EI}{p}\right)^{1/3} \int_{\bar{\kappa}_{min}}^{\bar{\kappa}} f(\bar{\kappa}; \bar{\kappa}_{min}, \bar{h}) d\bar{\kappa} & \text{for } AB \\ L - \left(\frac{EI}{p}\right)^{1/3} \int_0^{\bar{\kappa}} f(\bar{\kappa}; \bar{\kappa}_{min}, \bar{h}) d\bar{\kappa} & \text{for } BC \end{cases}, \quad (19)$$

where $\bar{\kappa} = [EI/(8p)]^{1/3}\kappa$, L is the length of the bent beam, and is given by

$$L = \left(\frac{EI}{p}\right)^{1/3} \int_{\bar{\kappa}_{min}}^{\bar{\kappa}_{max}} f(\bar{\kappa}; \bar{\kappa}_{min}, \bar{h}) d\bar{\kappa} + \left(\frac{EI}{p}\right)^{1/3} \int_0^{\bar{\kappa}_{max}} f(\bar{\kappa}; \bar{\kappa}_{min}, \bar{h}) d\bar{\kappa}. \quad (20)$$

Fig. 4 shows the distribution of the normalized curvature $[EI/(8p)]^{1/3}\kappa$ in the beam (versus the normalized arc length $[8p/(EI)]^{1/3}s$) for $\bar{h} = 0$, 0.798 and 2. The maximum curvature (in absolute value) for $\bar{h} = 0$ is slightly larger than that for $\bar{h} = 0.798$ and 2, where $\bar{h} = 0.798$ corresponds to the experiments (Kim et al., 2012a) (see Section 3 for details).

The angle of rotation can be obtained by integrating $d\theta = \kappa ds$ as

$$\theta(\bar{\kappa}) = \begin{cases} 2\int_{\bar{\kappa}_{min}}^{\bar{\kappa}} \bar{\kappa} f(\bar{\kappa}; \bar{\kappa}_{min}, \bar{h}) d\bar{\kappa} + \frac{\pi}{2} & \text{for } AB \\ -2\int_0^{\bar{\kappa}} \bar{\kappa} f(\bar{\kappa}; \bar{\kappa}_{min}, \bar{h}) d\bar{\kappa} & \text{for } BC \end{cases}. \quad (21)$$

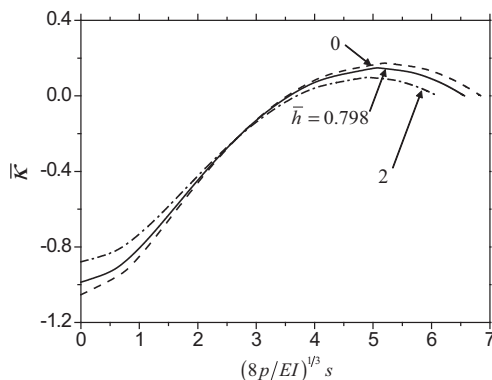The profile (x, y) can also be obtained analytically by integrating $dx = \cos\theta ds$ and $dy = \sin\theta ds$ as

Fig. 4. The curvature distribution in the beam for several normalized beam thickness.

$$x(\bar{\kappa}) = \left(\frac{EI}{p}\right)^{1/3} \begin{cases} \int_{\bar{\kappa}_{min}}^{\bar{\kappa}} \cos[\theta(\bar{\kappa})] f(\bar{\kappa}; \bar{\kappa}_{min}, \bar{h}) d\bar{\kappa} & \text{for } AB \\ \frac{\bar{x}_C}{2} - \int_0^{\bar{\kappa}} \cos[\theta(\bar{\kappa})] f(\bar{\kappa}; \bar{\kappa}_{min}, \bar{h}) d\bar{\kappa} & \text{for } BC \end{cases}$$

$$y(\bar{\kappa}) = \left(\frac{EI}{p}\right)^{1/3} \begin{cases} \int_{\bar{\kappa}_{min}}^{\bar{\kappa}} \sin[\theta(\bar{\kappa})] f(\bar{\kappa}; \bar{\kappa}_{min}, \bar{h}) d\bar{\kappa} & \text{for } AB \\ \frac{\bar{h}}{4} - \int_0^{\bar{\kappa}} \sin[\theta(\bar{\kappa})] f(\bar{\kappa}; \bar{\kappa}_{min}, \bar{h}) d\bar{\kappa} & \text{for } BC \end{cases}, \quad (22)$$

where $\bar{x}_C = 2\int_{\bar{\kappa}_{min}}^{\bar{\kappa}_{max}} \cos[\theta(\bar{\kappa})] f(\bar{\kappa}; \bar{\kappa}_{min}, \bar{h}) d\bar{\kappa} + 2\int_0^{\bar{\kappa}_{max}} \cos[\theta(\bar{\kappa})] f(\bar{\kappa}; \bar{\kappa}_{min}, \bar{h}) d\bar{\kappa}$. Fig. 5 shows the normalized "tennis racket" shape, $[8p/(EI)]^{1/3}y$ versus $[8p/(EI)]^{1/3}x$ from above equation, for $\bar{h} = 0.798$. For comparison, Fig. 5 also shows the numerical results of the "tennis racket" shape obtained from FEA, which agrees well with the analytic model, as to be discussed in details in the next section.

3. Design of stretchable electronics on the balloon catheter

3.1. Maximum strains in the microelectrodes and interconnects

For a composite beam with multiple layers (e.g., Fig. 1e), the effective bending stiffness (per unit width) is given by

$$EI = \sum_{i=1}^n E_i h_i \left\{ \frac{h_i^2}{3} + \left[\left(\sum_{j=1}^i h_j\right) - h_{neutral}\right]^2 - h_i \left[\left(\sum_{j=1}^i h_j\right) - h_{neutral}\right] \right\}, \quad (23)$$

where the summation is for all n layers with $i = 1$ being the bottom layer, E_i and h_i are the Young's modulus and thickness of ith layer, and $h_{neutral}$ is the distance from the bottom to the neutral mechanical plane and is given by

$$h_{neutral} = \frac{\sum_{i=1}^n E_i h_i \left[\left(\sum_{j=1}^i h_j\right) - \frac{h_i}{2}\right]}{\sum_{i=1}^n E_i h_i}. \quad (24)$$

The Young's moduli of polyurethane, Dymax, PI and Au are 21 MPa, 60 MPa, 2.8 GPa and 78 GPa, respectively. For thicknesses of different layers described at the beginning of Section 2, Eq. (24) gives the bending stiffness (per unit width) for different cross sections as 6.67 μN·m with the microelectrode, 6.57 and 7.85 μN·m within and beyond the pair of microelectrodes, respectively (see Appendix A for details). These values are very close, which justifies the uniform beam model adopted in Section 2. For $EI = 7.85$ μN·m, the corresponding distance from the bottom to the neutral mechanical plane in Eq. (24) is $h_{neutral} = 85.4$ μm. This distance $h_{neutral}$ is equivalent to $h/2$ in Section 2, and therefore Eq. (18) becomes

$$\bar{\kappa}_{min} = -1.053 + 0.1628\bar{h}_{neutral},$$
$$\bar{\kappa}_{max} = 0.1745 - 0.05706\bar{h}_{neutral}. \quad (25)$$

The maximum strain in the microelectrodes or interconnects must be less than the failure strain ε_f ($\sim$ a few percents), i.e.,
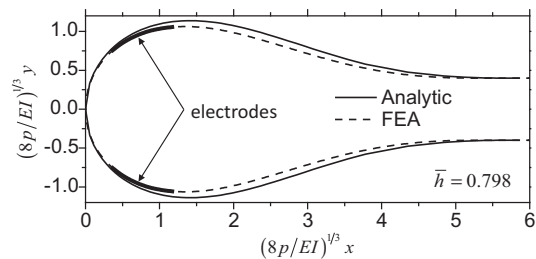

Fig. 5. The normalized "tennis racket" profiles obtained from the analytic model and FEA.

$$\varepsilon_{\max} = |\kappa| d_{\max} = 2\left(\frac{p}{EI}\right)^{1/3} |\bar{\kappa}| d_{\max} < \varepsilon_f, \tag{26}$$

where the curvature κ (or $\bar{\kappa}$) is given in Eq. (19) and also Fig. 4, $d_{\max}$ is the maximum distance between the microelectrodes (or interconnects) and the neutral mechanical plane, and $d_{\max} = 3.30\,\mu m$ and $0.631\,\mu m$ for the cross sections with microelectrodes and interconnects, respectively. For the pair of microelectrodes with spacing $750\,\mu m$, the curvature is $2.51\,mm^{-1}$ from Fig. 4 for $p = 1$ atm and $s = 750\,\mu m/2$, which gives the maximum strain in Au 0.83% in the microelectrodes. The interconnects cover the entire equator of balloon catheter and have the maximum curvature $4.61\,mm^{-1}$ at $s = 0$, which gives the maximum strain in Au 0.29% in the interconnects. Eqs. (24)–(26) can be used to reduce the maximum strain $\varepsilon_{\max}$ in the microelectrodes or interconnects for optimal design of balloon catheter. The thicknesses of the multiple-layer structure can be optimized to reduce d_{max} via Eq. (24) and the curvature κ via Eq. (25).

3.2. Radius of inflated balloon catheter

The microelectrodes and interconnects are fabricated on a flat state. After they are transfer printed onto the inflated balloon catheter with radius $R_{balloon}$, the maximum bending strain in Au is given by

$$\varepsilon_{\max} = \frac{d'_{\max}}{R_{balloon}}, \tag{27}$$

where $d'_{\max}$ is the maximum distance between the microelectrodes (or interconnects) and the neutral mechanical plane of the cross section without the balloon catheter. Similar to Eq. (24), this neutral mechanical plane is characterized by the distance

$$h'_{neutral} = \frac{\sum_{i=2}^{n} E_i h_i \left[\left(\sum_{j=2}^{i} h_j\right) - \frac{h_i}{2}\right]}{\sum_{i=2}^{n} E_i h_i}, \tag{28}$$

where the summation starts from $i = 2$ (without the balloon catheter). For the cross sections with microelectrodes and interconnects,

$d'_{\max} = 1.14\,\mu m$ and $2.51\,\mu m$, respectively. For the radius $R_{balloon} = 1$ cm of inflated balloon catheter as in experiments, Eq. (27) gives the maximum strain in Au 0.011% in the microelectrodes and 0.025% in the interconnects, which are negligible as compared to the maximum strains during deflation of the balloon catheter. Only when the radius of inflated balloon catheter is as small as $250\,\mu m$ the maximum strain in Au before deflation reaches 1%.

The microelectrodes and interconnects printed on the inflated balloon catheter have an initial curvature $-1/R_{balloon}$ prior to the external pressure p. It can be shown that the analysis in Section 2 still holds if its curvature κ is understood as the total curvature. Therefore $\kappa + (1/R_{balloon})$ represents the curvature due to p. The strain in the microelectrodes and interconnects is the sum of the strains due to initial curvatures [e.g., Eq. (27)] and external pressure [e.g., Eq. (26)]. Its maximum can then be estimated as

$$\varepsilon_{\max} \leqslant \frac{d'_{\max}}{R_{balloon}} + \left|\left(\frac{8p}{EI}\right)^{1/3}\bar{\kappa} + \frac{1}{R_{balloon}}\right| d_{\max}, \tag{29}$$

where the normalized curvature $\bar{\kappa}$ is obtained from Eq. (19).

3.3. Finite element analysis

Finite element analysis is used to validate the basic assumptions of a uniform, initial flat beam in the analytic model in Section 2. It accounts for the non-uniform cross sections of multiple layers discussed in Section 3.1. The effects of radius of inflated balloon catheter and pre-stress in the microelectrodes and interconnects are also accounted for. Fig. 5 shows profile of deflated balloon catheter obtained by the two-dimension FEA, which models different cross sections by a beam with non-uniform bending stiffness subject to the external pressure on one side of the beam. The positions of electrodes on the deflated balloon catheter are clearly marked. The overall profiles of deflated balloon catheter obtained by the analytic model and FEA agree well.

Three-dimensional FEA is also used to model the entire balloon catheter, including the large polyurethane part not covered by the microelectrodes and interconnects, all subject to external pressure. The balloon catheter is modeled by the shell element in the ABAQUS finite element program (Dassault-Systèmes, 2010). Effective bending and tensile stiffnesses, which are the same to the structure in the experiment, are assigned for both the equator and the large polyurethane part. The two ends are fixed on the corresponding positions of the surface of a rigid cylinder, which simulates the bar of the balloon catheter as shown in Figs. 1a and 1b. Contact between the balloon and the bar and self-contact of the balloon are considered during the process of loading. Fig. 6a shows the deflated balloon catheter, with the strip clearly indicating the microelectrodes and interconnects. Fig. 6b shows that the overall profiles of deflated balloon catheter obtained by 3D FEA agrees reasonably well with the analytic model.

4. Concluding remarks

Stretchable electronics is applied to balloon catheters for high-efficacy ablation, with tactile sensing integrated on the surface, to establish full and conformal contact with the endocardial surface for elimination of the heart sink caused by blood flow around their surfaces. The balloon catheter, on which microelectrodes and interconnects are printed, undergoes extreme mechanical deformation during its inflation and deflation. An analytic solution is obtained for balloon catheter inflation and deflation, which gives analytically the distribution of curvatures and the maximum strain in the microelectrodes and interconnects, and accounts for the radius of inflated balloon catheter. The analytic solution is validated by the finite element analysis.
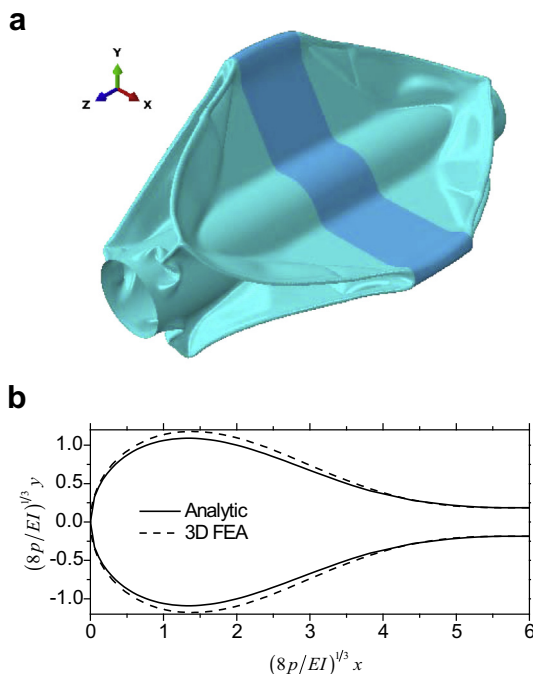

Fig. 6. (a) The deflated balloon catheter simulated by 3D FEA; (b) the normalized "tennis racket" profiles obtained from the analytic model and 3D FEA.

Acknowledgements

Appendix A

Boundary condition in Eq. (8)

Let $\tilde{N} = N\cos\theta - V\sin\theta$ and $\tilde{V} = V\cos\theta + N\sin\theta$ denote the forces in the x and y directions, respectively. Their substitution into Eqs. (1b,c) yields $\cos\theta d\tilde{V}/ds - \sin\theta d\tilde{N}/ds - p = 0$ and $\cos\theta d\tilde{N}/ds + \sin\theta d\tilde{V}/ds = 0$. Elimination of $\tilde{V}$ gives

$$\frac{d\tilde{N}}{ds} + p\sin\theta = 0, \tag{A.1}$$

Together with the geometric relation $\sin\theta = dy/ds$, integration of the above equation gives

$$\tilde{N} + py = \text{constant}. \tag{A.2}$$

At the symmetry point A, Eq. (5b,c) lead to $\tilde{N} = 0$, which together with Eq. (5a), gives a vanishing constant Eq. (A.2), i.e., $\tilde{N} + py = 0$. At point C, Eq. (6b) leads to $\tilde{N} = N = N_0$, which together with Eq. (6a), gives Eq. (8).

Perturbation solution

It can be shown, via Eq. (15), that the function defined in Eq. (17) satisfies $f(\bar{\kappa}; \bar{\kappa}_{\min}, \bar{h}) = f(\bar{\kappa}; \bar{\kappa}_{\max}, \bar{h})$. Eq. (16) can then be written as

$$\int_{\bar{\kappa}_{\min}}^{0} \bar{\kappa} f(\bar{\kappa}; \bar{\kappa}_{\min}, \bar{h}) d\bar{\kappa} + 2\int_{0}^{\bar{\kappa}_{\max}} \bar{\kappa} f(\bar{\kappa}; \bar{\kappa}_{\max}, \bar{h}) d\bar{\kappa} = -\frac{\pi}{4}. \tag{A.3}$$

By the change of integration variable, the above equation can be rewritten as

$$\int_{0}^{\sqrt{-\bar{\kappa}_{\min}}} \frac{(\bar{\kappa}_{\min} + \lambda^2) d\lambda}{\sqrt{-(2\bar{\kappa}_{\min} + \lambda^2)(2\bar{\kappa}_{\min}^2 + 2\bar{\kappa}_{\min}\lambda^2 + \lambda^4 + \bar{h}/4) - 1}}$$
$$+ 2\int_{0}^{\sqrt{\bar{\kappa}_{\max}}} \frac{(\bar{\kappa}_{\max} - \lambda^2) d\lambda}{\sqrt{(2\bar{\kappa}_{\max} - \lambda^2)(2\bar{\kappa}_{\max}^2 - 2\bar{\kappa}_{\max}\lambda^2 + \lambda^4 + \bar{h}/4) + 1}} = -\frac{\pi}{8},$$

which, together with Eq. (15), give the governing equations for $\bar{\kappa}_{\min}$ and $\bar{\kappa}_{\max}$. For small $\bar{h}$, the perturbation method gives

$$\bar{\kappa}_{\min} = \bar{\kappa}_{\min(0)} + \bar{h}\bar{\kappa}_{\min(1)} + \cdots$$
$$\bar{\kappa}_{\max} = \bar{\kappa}_{\max(0)} + \bar{h}\bar{\kappa}_{\max(1)} + \cdots. \tag{A.5a, b}$$

The leading terms of $\bar{h}$, after the above equation is substituted into Eqs. (15) and (A.4), give

$$\bar{\kappa}_{\max(0)}^4 - \bar{\kappa}_{\min(0)}^4 + \bar{\kappa}_{\max(0)} - \bar{\kappa}_{\min(0)} = 0, \tag{A.6}$$

$$\int_{0}^{\sqrt{-\bar{\kappa}_{\min(0)}}} \frac{(\bar{\kappa}_{\min(0)} + \lambda^2) d\lambda}{\sqrt{-(2\bar{\kappa}_{\min(0)} + \lambda^2)(2\bar{\kappa}_{\min(0)}^2 + 2\bar{\kappa}_{\min(0)}\lambda^2 + \lambda^4) - 1}}$$
$$+ 2\int_{0}^{\sqrt{\bar{\kappa}_{\max(0)}}} \frac{(\bar{\kappa}_{\max(0)} - \lambda^2) d\lambda}{\sqrt{(2\bar{\kappa}_{\max(0)} - \lambda^2)(2\bar{\kappa}_{\max(0)}^2 - 2\bar{\kappa}_{\max(0)}\lambda^2 + \lambda^4) + 1}} = -\frac{\pi}{8}. \tag{A.7}$$

which have the numerical solution $\bar{\kappa}_{\min(0)} = -1.053$ and $\bar{\kappa}_{\max(0)} = 0.1745$. The next-order terms of $\bar{h}$, after Eq. (A.5a,b) is substituted into Eqs. (15) and (A.4), give

$$14.67\bar{\kappa}_{\min(1)} + 4.085\bar{\kappa}_{\max(1)} = 1.078, \tag{A.8}$$

$$1.842\bar{\kappa}_{\min(1)} - 3.261\bar{\kappa}_{\max(1)} = 0.2430, \tag{A.9}$$

which have the solution $\bar{\kappa}_{\min(1)} = 0.08143$ and $\bar{\kappa}_{\max(1)} = -0.02853$.

Effective. properties

As shown in Fig. 1a, most area of the equator (width 5 mm) is covered by the adhesive, which has the bending stiffness 7.83 μN·m obtained from Eq. (24). The interconnect, which has the bending stiffness 8.81 μN·m, covers the entire equator but at a smaller width (0.09 mm). The microelectrodes and the region within the pair of microelectrodes have the same width 1.5 mm, and their bending stiffness are 3.90 μN·m and 3.58 μN·m, respectively. The effective bending stiffness for each cross section in Section 3 can then be obtained by the weighted average according to the width.

References

Baek, J.-Y., An, J.-H., Choi, J.-M., Park, K.-S., Lee, S.-H., 2008. Flexible polymeric dry electrodes for the long-term monitoring of ECG. Sens. Actuators A-Phys. 143, 423–429.

Berger, T.W., Baudry, M., Brinton, R.D., Liaw, J.S., Marmarelis, V.Z., Park, A.Y., Sheu, B.J., Tanguay, A.R., 2001. Brain-implantable biomimetic electronics as the next era in neural prosthetics. Proc. IEEE 89, 993–1012.

Buehler, M.J., 2006. Mesoscale modeling of mechanics of carbon nanotubes: self-assembly, self-folding, and fracture. J. Mater. Res. 21, 2855–2869.

Buehler, M.J., Kong, Y., Gao, H.J., 2004. Deformation mechanisms of very long single-wall carbon nanotubes subject to compressive loading. J. Eng. Mater-T. Asme. 126, 245–249.

Dassault-Systèmes, 2010. Abaqus analysis user's manual v. 6.10. (Dassault Systèmes Simulia Corp., Rhode Island).

Elliott, J.A., Sandler, J.K.W., Windle, A.H., Young, R.J., Shaffer, M.S.P., 2004. Collapse of single-wall carbon nanotubes is diameter dependent. Phys. Rev. Lett. 92.

Falvo, M.R., Clary, G.J., Taylor, R.M., Chi, V., Brooks, F.P., Washburn, S., Superfine, R., 1997. Bending and buckling of carbon nanotubes under large strain. Nature 389, 582–584.

Fertis, D.G., 1999. Nonlinear Mechanics, second ed. CRC PressINC, New York.

Jin, H.C., Abelson, J.R., Erhardt, M.K., Nuzzo, R.G., 2004. Soft lithographic fabrication of an image sensor array on a curved substrate. J. Vac. Sci. Technol. B 22, 2548–2551.

Jung, I., Xiao, J., Malyarchuk, V., Lu, C., Li, M., Liu, Z., Yoon, J., Huang, Y., Rogers, J.A., 2011. Dynamically tunable hemispherical electronic eye camera system with adjustable zoom capability. Proc. Natl. Acad. Sci. U.S.A 108, 1788–1793.

Kim, D.-H., Ghaffari, R., Lu, N., Wang, S., Lee, S.P., Keum, H., D'Angelo, R., Klinker, L., Su, Y., Lu, C., Kim, Y.-S., Ameen, A., Li, Y., Zhang, Y., de Graff, B., Hsu, Y.-Y., Liu, Z., Ruskin, J., Xu, L., Lu, C., Omenetto, F.G., Huang, Y., Mansour, M., Slepian, M.J., Rogers, J.A., 2012a. Electronic sensor and actuator webs for large-area complex geometry cardiac mapping and therapy. Proc. Natl. Acad. Sci. U.S.A 109, 19910–19915.

Kim, D.-H., Lu, N., Huang, Y., Rogers, J.A., 2012b. Materials for stretchable electronics in bioinspired and biointegrated devices. Mrs Bull. 37, 226–235.

Kim, D.-H., Lu, N., Ma, R., Kim, Y.-S., Kim, R.-H., Wang, S., Wu, J., Won, S.M., Tao, H., Islam, A., Yu, K.J., Kim, T.-I., Chowdhury, R., Ying, M., Xu, L., Li, M., Chung, H.-J., Keum, H., McCormick, M., Liu, P., Zhang, Y.-W., Omenetto, F.G., Huang, Y., Coleman, T., Rogers, J.A., 2011. Epidermal electronics. Science 333, 838–843.

Kim, D.-H., Viventi, J., Amsden, J.J., Xiao, J., Vigeland, L., Kim, Y.-S., Blanco, J.A., Panilaitis, B., Frechette, E.S., Contreras, D., Kaplan, D.L., Omenetto, F.G., Huang, Y., Hwang, K.-C., Zakin, M.R., Litt, B., Rogers, J.A., 2010a. Dissolvable films of silk fibroin for ultrathin conformal bio-integrated electronics. Nat. Mater. 9, 511–517.

Kim, D.-H., Xiao, J., Song, J., Huang, Y., Rogers, J.A., 2010b. Stretchable, curvilinear electronics based on inorganic materials. Adv. Mater. 22, 2108–2124.

Ko, H.C., Stoykovich, M.P., Song, J., Malyarchuk, V., Choi, W.M., Yu, C.-J., Geddes III, J.B., Xiao, J., Wang, S., Huang, Y., Rogers, J.A., 2008. A hemispherical electronic eye camera based on compressible silicon optoelectronics. Nature 454, 748–753.

Lumelsky, V.J., Shur, M.S., Wagner, S., 2001. Sensitive skin sensors. J. IEEE 1, 41–51.

Mannsfeld, S.C.B., Tee, B.C.K., Stoltenberg, R.M., Chen, C.V.H.H., Barman, S., Muir, B.V.O., Sokolov, A.N., Reese, C., Bao, Z., 2010. Highly sensitive flexible pressure sensors with microstructured rubber dielectric layers. Nat. Mater. 9, 859–864.

Pugno, N.M., 2010. The design of self-collapsed super-strong nanotube bundles. J. Mech. Phys. Solids 58, 1397–1410.

Rogers, J.A., Huang, Y., 2009. A curvy, stretchy future for electronics. Proc Natl. Acad. Sci. U.S.A 106, 10875–10876.

Someya, T., Kato, Y., Sekitani, T., Iba, S., Noguchi, Y., Murase, Y., Kawaguchi, H., Sakurai, T., 2005. Conformable, flexible, large-area networks of pressure and thermal sensors with organic transistor active matrixes. Proc Natl. Acad. Sci. U.S.A 102, 12321–12325.

Someya, T., Sekitani, T., 2009. Printed skin-like large-area flexible sensors and actuators. In: Brugger, J., Briand, D. (Eds.), Proceedings of the Eurosensors Xxiii Conference. Elsevier Science Bv, Amsterdam, pp. 9–12.

Takei, K., Takahashi, T., Ho, J.C., Ko, H., Gillies, A.G., Leu, P.W., Fearing, R.S., Javey, A., 2010. Nanowire active-matrix circuitry for low-voltage macroscale artificial skin. Nat. Mater. 9, 821–826.

Timoshenko, S.P., Gere, J.M., 1961. Theory of elastic stability, second ed. McGraw-Hill, New York, USA.

Viventi, J., Kim, D.-H., Moss, J.D., Kim, Y.-S., Blanco, J.A., Annetta, N., Hicks, A., Xiao, J., Huang, Y., Callans, D.J., Rogers, J.A., Litt, B., 2010a. A conformal, bio-interfaced class of silicon electronics for mapping cardiac electrophysiology. Sci. Transl. Med. 2, 24ra22.

Viventi, J., Kim, D.-H., Moss, J.D., Kim, Y.-S., Blanco, J.A., Annetta, N., Hicks, A., Xiao, J., Huang, Y., Callans, D.J., Rogers, J.A., Litt, B., 2010b. A conformal, bio-interfaced class of silicon electronics for mapping cardiac electrophysiology. Sci. Transl. Med. 2.

Viventi, J., Kim, D.-H., Vigeland, L., Frechette, E.S., Blanco, J.A., Kim, Y.-S., Avrin, A.E., Tiruvadi, V.R., Hwang, S.-W., Vanleer, A.C., Wulsin, D.F., Davis, K., Gelber, C.E., Palmer, L., Van der Spiegel, J., Wu, J., Xiao, J., Huang, Y., Contreras, D., Rogers, J.A., Litt, B., 2011. Flexible, foldable, actively multiplexed, high-density electrode array for mapping brain activity in vivo. Nat. Neurosci. 14, 1599-U1138.

Zhou, W., Huang, Y., Liu, B., Hwang, K.C., Zuo, J.M., Buehler, M.J., Gao, H., 2007. Self-folding of single- and multiwall carbon nanotubes. Appl. Phys. Lett. 90.